NANO LETTERS

2008
Vol. 8, No. 4
1055-1060

A Triple Quantum Dot in a Single-Wall Carbon Nanotube

K. Grove-Rasmussen,*,†,‡ H. I. Jørgensen,‡ T. Hayashi,† P. E. Lindelof,‡ and T. Fujisawa†

NTT Basic Research Laboratories, NTT Corporation, 3-1 Morinosato Wakamiya, Atsugi-shi, Kanagawa 243-0198, Japan, and Nano-Science Center, Niels Bohr Institute, University of Copenhagen, Universitetsparken 5, 2100 Copenhagen Ø, Denmark

Received November 11, 2007; Revised Manuscript Received January 22, 2008

ABSTRACT

A top-gated single-wall carbon nanotube is used to define three coupled quantum dots in series between two electrodes. The additional electron number on each quantum dot is controlled by top-gate voltages allowing for current measurements of single, double, and triple quantum dot stability diagrams. Simulations using a capacitor model including tunnel coupling between neighboring dots captures the observed behavior with good agreement. Furthermore, anticrossings between indirectly coupled levels and higher order cotunneling are discussed.

Carbon nanotubes (CNTs), a promising material for quantum information devices,[1,2] are one-dimensional systems with remarkable coherency of electrons. It is therefore attractive to electrostatically define quantum dots, also known as artificial atoms, along the length of the CNT. Electron transport through a two-atomic molecule[3] consisting of two coupled quantum dots in a CNT[1,4–9] probes molecular states in which the electron is delocalized over the two quantum dots. Scaling the system further up to three coupled quantum dots[10,11] or a triatomic artificial molecule enables the study of more intriguing phenomena related to electrostatics[12–14] and molecular states of the triple quantum dot (quantum superposition of three levels). Coupled three-level systems might allow for future experiments inspired by the field of quantum optics[15–19] and are also attractive from a quantum information point of view.[20,21] In contrast to GaAs defined triple quantum dots, which can be (or sometimes unintentionally are) arranged in a triangular configuration,[19,22–27] the CNT geometry ensures the serial and simplest configuration, where electrons only tunnel between neighboring dots. Furthermore, the more challenging experiments of investigating the serial triple quantum dot Kondo effect[28] are yet to be addressed experimentally.

In this Letter we present measurement on a top-gated single-wall carbon nanotube showing individual control of three coupled quantum dots defined between the source and drain electrodes. The characteristics are understood as transport through molecular states rather than sequential tunneling through three dots. Charging effects with different capacitive and tunnel couplings between neighboring quantum dots are investigated by an electrostatic capacitor model including first-order tunneling processes. Finally, a discussion of triple quantum dot characteristics as second order anticrossings and higher order cotunneling is presented.

The devices are fabricated by an initial step to define Pt/Ti (40 nm/5 nm) alignment marks on top of a SiO_2 capped (500 nm) highly doped Si substrate. Subsequently, catalyst islands of iron nitrate ($Fe(NO_3)_3$), molybdenum acetate ($MoO_2(CH_3COO)_2$), and aluminum oxide nanosized particles in methanol are deposited relative to the alignment marks. Single-wall carbon nanotubes are grown from the catalyst islands by chemical vapor deposition at 850–950 °C in a mixture of methane, argon, and hydrogen. Electrodes (Au/Ti) are defined some micrometers away from the catalyst islands in hope that one nanotube bridges the electrode gap.[9] Top-gate electrodes (8 nm of Al oxide followed by 10 nm of Al and 25 nm of Ti) are defined on top of the nanotube, and a final optical lithography step is used to make the bonding pads. A scanning electron micrograph of a similar device with a nanotube crossing the gap between the two electrodes is shown in Figure 1a.

Figure 1b schematically shows the cross section of the device. Three top-gates are defined (Tg1–3) between the source and drain electrodes contacting the nanotube. The tunnel rate between the drain/source electrode and the nanotube is $\Gamma_{d,s}$, which to some extent is determined by the choice of electrode material.[29–31] The choice of Ti for this device yields tunnel barriers high enough to obtain single electron tunneling characteristics (see below).

In the case of a semiconducting CNT, the backgate can adjust the electrochemical potential of the CNT into the

* Corresponding author: grove@will.brl.ntt.co.jp.
† NTT Basic Research Laboratories, NTT Corporation.
‡ Nano-Science Center, Niels Bohr Institute, University of Copenhagen.

10.1021/nl072948y CCC: $40.75
Published on Web 03/04/2008

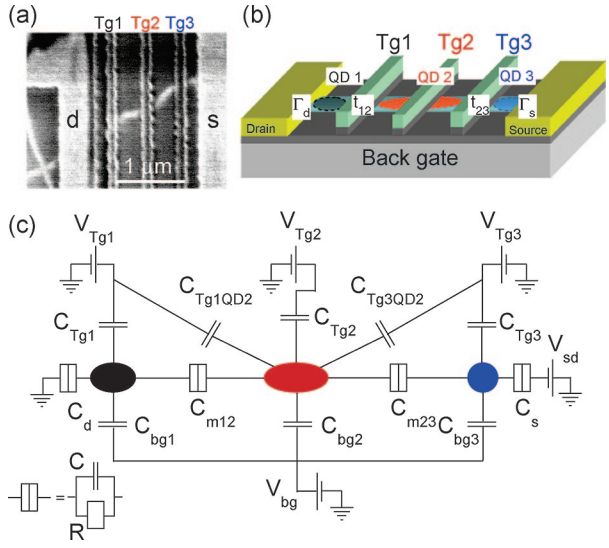

Figure 1. (a) Scanning electron micrograph (2 keV) of the central part of a similar device with the nanotube lying below three top-gates. (b) Schematic illustration of the device and the three serially coupled quantum dots formed due to the top-gates (black, red, and blue ovals). The tunnel rate at the nanotube/metal interfaces is given by $\Gamma_{d,s}$ and in this particular device tunnel couplings t_{12} and t_{23} are introduced below Tg1 and Tg3, respectively. (c) Electrostatic capacitance model including the most significant capacitances to model the observed behavior (see Figures 2 and 3). Tg1/3 tunes the electron number on QD1/3 and QD2, the latter effect represented by the cross capacitances. Furthermore, each nanotube quantum dot has capacitive coupling to the backgate.

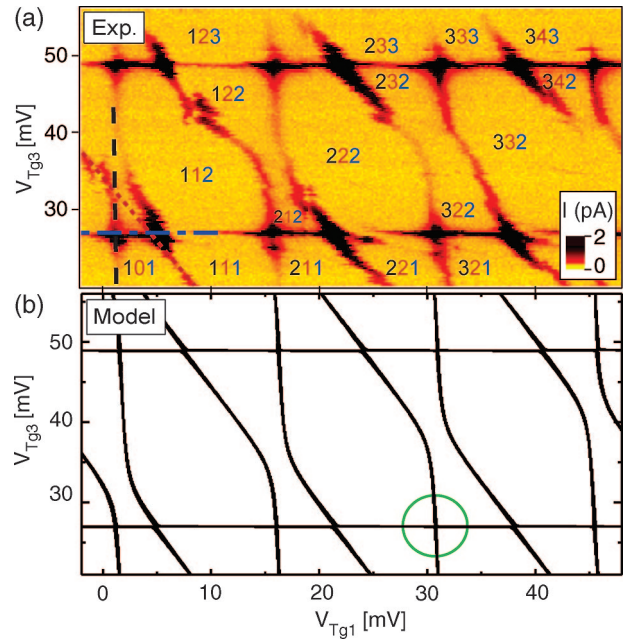

Figure 2. (a) Experiment: Current vs V_{Tg1} and V_{Tg3} probing the three quantum dots in the triple quantum dot ($T = 50$ mK, $V_{sd} = 50$ μV, $V_{bg} = 4$ V, $V_{Tg2} = 0$ V). Overall vertical, sloping, and horizontal lines are observed representing charge degeneracies between two charge states related to addition of an electron in QD1, QD2, and QD3, respectively. Strong and weak anticrossings are seen between QD1–2 and QD2–3, respectively. Charge states are indicated by additional electron number in the quantum dots. (b) Model: Stability diagram based on the capacitor model in Figure 1c including tunnel coupling between neighboring dots capturing the main features of the measurement in (a). See also Supporting Information.

valence/conduction band while the top-gates can introduce barriers below the gates by locally tuning the electrochemical potential into the band gap. By inducing tunnel barriers under selected top-gate electrodes, several quantum dot structures can be imagined as, e.g., a (tunable) single, double, triple, or even quadruple quantum dot. However, sometimes barriers are formed at zero gate voltage probably due to defects introduced during the electron beam lithography or evaporation process. In this particular device, tunnel barriers are formed under the two outermost top-gates (Tg1 and Tg3) but not under the central top-gate (Tg2), as evidenced from the following measurements. Each top-gate controls the electrostatic potential of (some of) the quantum dots, QD1, QD2, and QD3, while the tunnel barriers are less affected. The obtained triple quantum dot is illustrated in Figure 1b with the different colored ovals showing the position of the three quantum dots (black, red, and blue). The electrostatic behavior is captured in Figure 1c, where the device is represented by a capacitance model with tunnel coupling between neighboring dots. Negligible direct capacitive coupling between QD1 and QD3 is expected for the serial geometry. Furthermore, cross capacitances are inserted as deduced from measurements below, and capacitive coupling to the backgate is included.

In the sequential tunneling regime with very high barriers, transport through the triple quantum dot is only allowed at certain quadruple points in the three-dimensional gate space spanned by V_{Tg1}, V_{Tg2}, and V_{Tg3}, where four charge states are degenerate.[14] However, we observe large cotunneling current in a wide region of gate space, which can be interpreted as transport through molecular states of the triple quantum dot. The interdot tunnel couplings (t_{12} and t_{23}) formed under the top-gates are strong enough to form a coherent superposition (molecular state) over the triple dot, which is weakly coupled to the Ti source/drain electrodes.

Figure 2a shows the current through the triple quantum dot versus Tg1 and Tg3 with constant voltage on Tg2 at finite bias voltage having (overall) vertical, sloping, and horizontal lines. Examples are shown by black (dashed), red (dotted), and blue (dash-dotted) lines in the lower left of the figure.[34] The vertical, sloping, and horizontal lines correspond to adding an electron to QD1, QD2, and QD3, respectively. It is seen that sweeping only Tg1 adds electrons to QD1 (crossing vertical lines) and QD2 (crossing sloping lines), while sweeping only Tg3 adds electrons to QD2 (crossing sloping lines) and QD3 (crossing horizontal lines). Tg1/3 therefore couples capacitively to both QD1/3 and QD2 as schematically drawn in Figure 1c. The charge states $N_1N_2N_3$ are shown in the plot, where N_i is the additional electron number in QDi, $i = 1, 2, 3$. The observed behavior can, however, not solely be explained by electrostatics (without coupling). A relative large tunnel and capacitive coupling is seen at (anti)crossings between sloping and vertical lines in contrast to the crossings between sloping and horizontal lines. Thus the capacitive (C_{m12}) and tunnel coupling (t_{12}) between QD1 and QD2 are relatively large compared to the capacitive C_{m23} and tunnel coupling t_{23} between QD2 and QD3

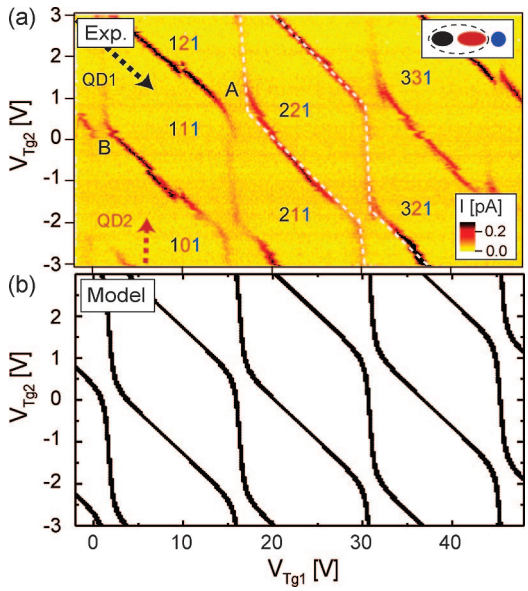

Figure 3. Experiment: Current vs V_{Tg1} and V_{Tg2} at $V_{bg} = 4$ V, $V_{sd} = 50$ μV and $T = 50$ mK of the double quantum dot formed by QD1 and QD2 as shown in the inset. QD3 is held in Coulomb blockade ($V_{Tg3} = 16$ mV). A clear (tilted) honeycomb pattern indicated by white dashed lines is seen showing two strongly coupled quantum dots and revealing a significant (negligible) cross capacitance from Tg1 to QD2 (Tg2 to QD1). The three colored numbers indicate the charge state of additional electron numbers in each QD. The red and black dotted arrows show the gate voltages for the single quantum dot measurements in Figure 4a,b. (b) Model: Calculation of the stability diagram of the double quantum dot within the triple quantum dot showing good agreement with the experiment ($V_{Tg3}^{model} = 16$ mV, i.e., Coulomb blockade). See Supporting Information for more details.

(DQD23). Furthermore, the direct capacitive coupling between QD1 and QD3 is as expected small because a crossing behavior is observed between horizontal and vertical lines. Since an electron cannot tunnel from QD1 to QD3, no direct tunnel coupling between QD1 and QD3 exists in contrast to the triangular triple quantum dot geometry. This crossing will be subject for further discussion below.

We can also probe a more familiar charging effect on a double quantum dot formed by QD1 and QD2 (DQD12). Figure 3a shows the current through the triple quantum dot versus Tg1 and Tg2 at finite bias voltage. The voltage on Tg3 is fixed leaving QD3 in Coulomb blockade with a constant number of electrons. A (tilted) honeycomb pattern is revealed as expected for a double quantum dot with finite current primarily along sloping and vertical lines due to electrostatics. Crossing the vertical lines corresponds to adding an electron to QD1, while crossing the sloping lines similarly corresponds to adding an electron to QD2. When Tg1 is increased and Tg2 remains constant, both vertical and sloping lines are crossed indicating a capacitive coupling from Tg1 to both QD1 and QD2, respectively, as deduced above as well (Figure 2). In contrast only sloping lines are crossed when increasing Tg2 for constant Tg1 illustrating that there is no cross capacitance from Tg2 to QD1 (thus part of the deduced schematics in Figure 1c). Consistent with Figure 2a, the strong anticrossings observed between sloping and horizontal lines reveals the presence of a significant electrostatic (C_{m12}) and tunnel coupling (t_{12}) between QD1 and QD2. This indicates that transport involves molecular ground states, e.g., the transport around A (lower wing) is due to a degeneracy between the 111 charge state and the ground-state of the quantum superposition involving the 121 and 211 charge states. Some variation in the tunnel and capacitive coupling is observed, e.g., stronger coupling between the 211 and the 121 states (anticrossing at A) than between the 101 and 011 states (anticrossing at B).

We can also investigate each single QD by sweeping the top-gate voltages, for example along the black or red dashed arrows in Figure 3a for the measurement of QD1 and QD2, respectively. Similarly, QD3 can be probed as well (not shown).[35] Figure 4b shows the stability diagram of QD2 by adjusting the electrochemical potentials of QD2 only (see Figure 4e) via Tg2. It reveals clear Coulomb blockade diamonds due to addition of electrons in QD2 with an addition energy of $E_{add2} \sim 3.5$ meV and excited states with a level spacing of $\Delta E_2 \sim 0.7$ meV (see arrow and vertical bar, respectively). Similarly, the stability diagram of QD3 in Figure 4c shows well-defined Coulomb blockade diamonds with an estimated addition energy of $E_{add3} \sim 12$ meV (blue arrow) and a less clear level spacing around $\Delta E_3 \sim 1$–2 meV. However, additional horizontal lines are visible at low finite bias attributed to transport through molecular states primarily related to the electron being localized in QD2 (i.e., source or drain chemical potentials being aligned with (red) electrochemical potentials of QD2 in Figure 4f). The bias gap between the highest negative and lowest positive lines therefore corresponds to the addition energy of QD2 scaled by a capacitance dependent factor α indicated by the black arrow in Figure 4a−c. Finally, the stability diagram of QD1 is shown in Figure 4a exhibiting a less regular behavior. The Coulomb diamonds are cutoff at finite bias due to tunneling through molecular states as the case of QD3, which makes it more difficult to estimate the addition energy. An estimate of diamond (2,1,1) yields $E_{add1} \sim 6$ meV. Also in this case the scaled addition energy of QD2 matches the bias gap (black arrow) between lowest finite bias lines, and the fine structure at higher bias is in agreement with the level spacing of QD2. The bias voltage position of the finite bias lines in QD1 (Figure 4a) are shifted by changing voltage on Tg2, i.e., tuning the electrochemical potential (molecular states) of QD2 consistent with the above interpretation (not shown).

It should be noted that the transport characteristics are different from weakly coupled triple quantum dots in the sequential tunneling regime. Transport is allowed even when only one of the QDs is located in the transport window while others are in the Coulomb blockade regime. We observe larger current when two QDs are in the transport window as seen at the crossing points of conductance lines in Figure 2, and even larger current at the quadruple point (not shown). A more thorough discussion of the current in terms of cotunneling follows below. We also note that the observed characteristic of relatively strong interdot tunnel coupling is incompatible with transport through three parallel CNTs, since they only would be capacitively coupled. The molecular state interpretation of the triple dot measurements is further

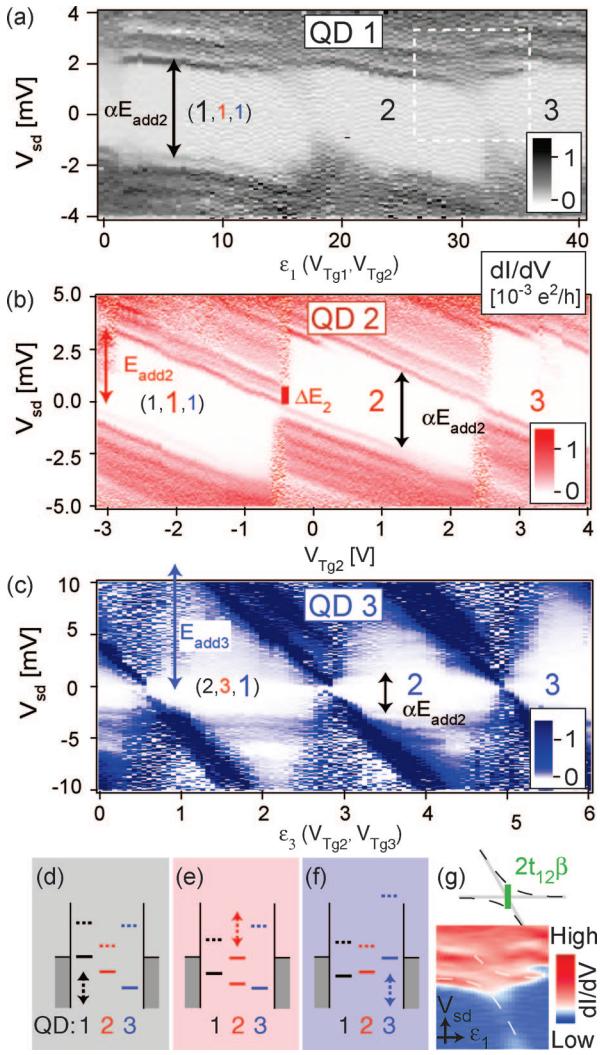

Figure 4. (a−c) Stability diagrams of QD1–3 (black, red, and blue dots in Figure 1b,c) showing that three single quantum dots are formed at $V_{bg} = 4$ V ($T = 50$ mK). The additional electron number in each dot is indicated in the center of the Coulomb blockade diamonds. Red and blue arrows indicate the addition energy of QD2 and QD3, while black arrows show the condition for finite bias transport through molecular states mostly belonging to QD2 in Coulomb blockade for QD1 and QD3 (α is a capacitance dependent factor). (d−f) Energy diagrams of the triple quantum dot showing the electrochemical potentials for adding electrons to the three dots. When the stability diagram of, e.g., QD1 is measured (d), the electrochemical potentials in QD2 and QD3 are held constant, while tuning the electrochemical potentials in QD1 up or down (indicated by dotted arrows). Similarly, QD2 and QD3 (e and f) can be probed. (g) Data from dashed square in QD1 (a) showing level crossing between levels in QD1 and QD2, i.e., the Coulomb blockade diamond edge (mainly level in QD1) anticrosses the horizontal lines (mainly level in QD2) (see schematics). Dashed and gray lines illustrate the behavior with and without coupling, respectively.

supported by the following calculation based on the capacitance model shown in Figure 1c. We try to estimate a reasonable set of parameters (12 capacitances and two tunnel couplings) by calculating stability diagrams of the capacitor circuit shown in Figure 1c including single electron tunneling processes within the triple quantum dot. The general features of the resulting stability diagram (the vertical, sloping and horizontal lines) are due to electrostatics, which are primarily

Table 1. Table Showing the Capacitances Used in the Model To Calculate the Stability Diagrams in Figure 2b and Figure 3b from Which the Charging/Coupling Energies Are Calculated[a]

i	C_i (aF)	i	C_i (aF)	i	C_i (aF)	i	C_i (aF)
Tg1	11	bg1	8.6	Tg1QD2	9.5	cm12	2
Tg2	0.05	bg2	28.5	Tg3QD2	6	cm23	0.2
Tg3	7.3	bg3	2.9	s	2.9	d	5

[a] Note, the low capacitance value of Tg2, an effect also observed in other devices with this geometry, probably due to some damage during the processing.

determined by the top-gate capacitances[3,14] (see Supporting Information S1). The deduced charging energies U_{c1}, U_{c2}, and U_{c3} from the single quantum dot measurements in Figure 4a−c depend on the total capacitance of each dot and are related to the capacitances of the model by (C_{m12}, $C_{m23} \ll C_{1,2,3}$)[14]

$$U_{c1} \simeq \frac{e^2}{C_1}\left(1 - \frac{C_{m23}^2}{C_2 C_3}\right) \quad (1)$$

$$U_{c2} \simeq \frac{e^2}{C_2} \quad (2)$$

$$U_{c3} \simeq \frac{e^2}{C_3}\left(1 - \frac{C_{m12}^2}{C_1 C_2}\right) \quad (3)$$

where C_i, $i = 1, 2, 3$, is the sum of the capacitances directly connected to QDi, i.e., $C_1 = C_s + C_{Tg1} + C_{bg1} + C_{m12}$, $C_2 = C_{m12} + C_{Tg2} + C_{bg2} + C_{m23} + C_{Tg1QD2} + C_{Tg3QD2}$, and $C_3 = C_d + C_{Tg3} + C_{bg3} + C_{m23}$ (see Supporting Information S1). The charging energies obtained and used in the model are $U_{c1} \simeq$ 6.0 meV, $U_{c2} \simeq$ 3.5 meV, and $U_{c3} \simeq$ 12.0 meV. As pointed out in the analysis of the measurements, the coupling between QD1 and QD2 is stronger than the coupling between QD2 and QD3, yielding coupling energies $U_{m12} \simeq$ 0.26 meV $> U_{m23} \simeq$ 0.05 meV (see Supporting Information). Geometrical considerations on the device structure are also used to estimate the backgate capacitances,[36] and the 12 capacitances are listed in Table 1.

Given all the capacitances in the model, electrostatic stability diagrams can be calculated[14] by finding the charge (ground) state (N_1, N_2, N_3) having the lowest electrostatic energy $U_{N_1N_2N_3}$. When the tunnel couplings are included, the charge states with the same total number of electrons on the triple quantum dot couples together forming molecular states (e.g., $N = 1$ (1,0,0), (0,1,0), and (0,0,1) couple together). The eigenenergies for a total electron number N on the triple quantum dot is found by diagonalizing the corresponding matrix with the diagonal elements given by the electrostatic energies $U_{N_1N_2N_3}$ and the off-diagonal elements being zero except when two charge states are connected by one tunneling event, e.g., (1,0,0) is connected with (0,1,0) by t_{12} and (0,1,0) is connected with (0,0,1) by t_{23}. When the molecular ground-state energy with a total number of N electrons on the triple quantum dot is equal to the ground-state energy with $N + 1$ electrons, transport is allowed. The model therefore describes the measurement by ground-state transport through molecular triple quantum dot states. More details are given in the Supporting Information S2.

Figure 2b shows the resulting plot, which resembles the main features of the measurement in Figure 2a with good

agreement.[37] The electrostatic part of the model captures the charging effects, while the tunnel part (and capacitive interdot coupling) makes strong/weak anticrossing behavior for DQD12/DQD23. We obtain tunnel couplings $t_{12} \sim 0.3$ meV and $t_{23} \lesssim 0.03$ meV from the analysis, where the tunnel coupling t_{23} is an upper bound. An estimate of the anticrossing between levels in QD1 and QD2 (t_{12}) can also be found from the bias stability diagram of QD1 shown in Figure 4a, e.g., in the dashed box shown in another color scheme in Figure 4g. The lower white dashed line in Figure 4g follows the edge of the Coulomb diamond (mainly a level in QD1), which makes an anticrossing with a horizontal line (mainly a level in QD2) as the bias is increased. See also Figure 4a, where no dashed guide lines are drawn. The schematic of this behavior is shown in the top panel of Figure 4g with the strength of the anticrossing being pure tunnel-like (i.e., no interdot capacitance). An estimate along the bias direction (green bar) yields $t_{12} \sim 0.35$ meV in agreement with the average value obtained from the model. The capacitance-dependent factor β is in this case close to 1, since the electrochemical potentials in QD1 are only little affected by changing the voltage on the source. A more complicated anticrossing behavior involving excited states is also observed at higher bias voltage. Finally, the model also describes the measurements when sweeping another set of top-gates as, e.g., shown in Figure 3a,b for DQD12. Since Tg1 and Tg2 do not couple to QD3, a well-coupled double quantum dot honeycomb structure is observed consistent with the triple quantum dot stability diagram. A double quantum dot DQD23 is also formed between QD2 and QD3, which shows very weak anticrossings as expected (not shown) from the above measurement.

The model presented here is the simplest approach to a coupled triple quantum dot ignoring shell structure, spin, and the effect of hybridization to the leads. The shell structure is to some extent visible in the measurement, since the addition energies are not constant throughout the gate sweeps shown. This is supported by the single QD stability diagrams, where excited states are observed (Figure 4). However, the shell structure is unfortunately not clear enough to assign even/odd or 4-fold electron occupation for the filling. These effects are therefore not included in the model in the simplest approach. In the case of clear shell structure, an interesting topic would be to study exchange interaction in the triple quantum dot system. The model assumes constant (average) tunnel and capacitive couplings even though the coupling between the different charge states (orbitals) varies in the measurements as mentioned.

We will end by briefly discussing two phenomena in triple quantum dots based on the above model and experiment. We focus on a gate voltage region, where a vertical and a horizontal line cross as, e.g., marked by the green circle in the model calculation of Figure 2b and magnified in Figure 5a (black lines). The electrochemical potentials of QD1 and QD3 at the crossing are aligned with the chemical potential of the leads, while QD2 is in Coulomb blockade as shown in Figure 5c. The current profile along the vertical resonance line indicated by the blue arrow in Figure 5a is therefore

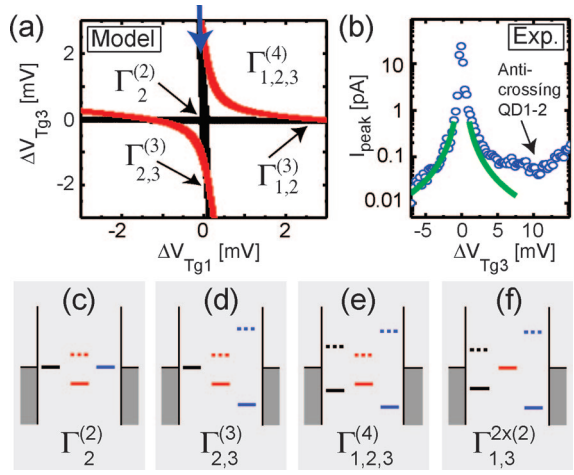

Figure 5. (a) Model: The crossing (black lines) and second-order anticrossing (red lines) correspond to having the electrochemical potential aligned in QD1 and QD3. Tunnel couplings $t_{12} = t_{23} =$ 0.5 meV are chosen large to increase clarity. Examples of gate regions with second (c), third (d), and fourth (e) order cotunneling rates $\Gamma_j^{(i)}$ with (i) being the order and j referring to the QD(s) in Coulomb blockade. (b) Measured peak current along the vertical (and for large positive ΔV_{Tg3} sloping) resonance line extracted from Figure 2a with the peak position marked by the green circle in Figure 2b. The green lines are best fit based on third-order cotunneling to the tails of the peak. (c−e) Energy diagrams showing the above-mentioned cotunneling configurations. (f) Another possible cotunneling process involving two consecutive second-order processes.

expected to be a single peak. This is confirmed in Figure 5b showing the measured peak current profile (blue circles) versus voltage on Tg3 extracted from Figure 2a, where $\Delta V_{Tg3} = 0$ is at the crossing. However, increasing the tunnel coupling (mainly t_{23}) in the model leads to a clear anticrossing (red lines in Figure 5a) even though no direct tunnel coupling between QD1 and QD3 exists. Such an anticrossing is therefore of second order, a phenomenon not possible to study in double quantum dots. The system has close analogy to a three-level system in the Λ-configuration, where intriguing experiments are expected.[15] Although the anticrossing is not resolved in our device, second or higher order cotunneling can be discussed in terms of elastic cotunneling rates $\Gamma_j^{(i)}$, where (i) is the order and j is the QD(s) in the Coulomb blockade. In the close vicinity of the above-discussed crossing, only QD2 is in Coulomb blockade (see Figure 5c), and the major contribution to the current therefore stems from second order cotunneling with rate $\Gamma_2^{(2)}$, yielding a relatively high current. Detuning the electrochemical potential of QD1 (QD3) along the horizontal (vertical) resonance line changes the order of the dominant cotunneling to third-order $\Gamma^{(3)}$ (black arrows in Figure 5a). The electrons now have to cotunnel through two neighboring QDs, i.e., QD2 and QD1 (QD3) as seen in Figure 5d for $\Gamma_{2,3}^{(3)}$. The current therefore decreases as illustrated by the peak in Figure 5b. The green lines show best fit (using the data for negative ΔV_{Tg3}) to the measurement $I \sim \Gamma_{2,3}^{(3)} \sim 1/\Delta V_{Tg3}^2$, which is the expected gate-dependence sufficiently far from resonance.[33] Here the third-order process is dominant and we assume negligible contribution due to the simultaneous change of the electrochemical potential of QD2, when

changing V_{Tg3}. A less good correspondence between the fit and the measurement is observed on the right side of the peak, which might be related to the strong anticrossing between QD1 and QD2 for positive ΔV_{Tg3} modifying the gate-dependence. For gate voltages outside the lines (white areas in Figure 5a), all QDs are in Coulomb blockade (Figure 5e). Current is then due to fourth-order cotunneling $\Gamma_{1,2,3}^{(4)}$ and therefore highly suppressed giving the stable charge configurations in the stability diagrams of Figure 2a and Figure 3a. For completeness, one additional type of process exists involving two second-order cotunneling $\Gamma_{1,3}^{2x(2)}$ corresponding to having only the electrochemical potential of QD2 at resonance (see Figure 5f). This process is more likely than third-order cotunneling[14] consistent with the higher current along sloping lines ($\Gamma_{1,3}^{2x(2)}$) than vertical lines ($\Gamma_{2,3}^{(3)}$) in the double quantum dot (DQD12) stability diagram shown in Figure 3a.

In conclusion we have shown measurement on a top-gated single-wall carbon nanotube interpreted as a serially coupled triple quantum dot formed between the source and drain electrodes. The stability diagram for single, double, and triple quantum dot(s) is observed by individual control of the electron number on each quantum dot via top-gate voltages. An electrostatic model describing ground-state transport involving triple quantum dot molecular states captures the main features of the double and triple quantum dot stability diagrams with good agreement. Finally, second-order anticrossings and cotunneling was discussed.

Acknowledgment. We thank Y. Hirayama for support of this joint collaboration and A. Fujiwara and Y. Ono for use of their equipment. Furthermore, we acknowledge the support of the EU-STREP Ultra-1D and CARDEQ programs. This work was also supported by the SCOPE from the Ministry of Internal Affairs and Communications of Japan, and by a Grant-in-Aid for Scientific Research from the JSPS.

Supporting Information Available: The derivation of the electrostatic energy used in the model is explained in detail together with the procedure to obtain stability diagrams without tunnel coupling (S1). Furthermore, the method to include tunnel coupling between neighboring quantum dots yielding the stability diagrams of the triple quantum dot shown in this Letter is addressed (S2). This material is available free of charge via the Internet at http://pubs.acs.org.

References

(1) Sapmaz, S.; Meyer, C.; Beliczynski, P.; Jarillo-Herrero, P.; Kouwenhoven, L. P. *Nano Lett.* **2006**, *6*, 1350.
(2) Loss, D.; DiVincenzo, D. P. *Phys. Rev. A* **1998**, *57*, 120.
(3) van der Wiel, W. G.; de Franceschi, S.; Elzerman, J. M.; Fujisawa, T.; Tarucha, S.; Kouwenhoven, L. P. *Rev. Mod. Phys.* **2002**, *75*, 1–22.
(4) Biercuk, M. J.; Mason, N.; Chow, J. M.; Marcus, C. M. *Nano Lett.* **2004**, *4*, 2499.
(5) Mason, N.; Biercuk, M. J.; Marcus, C. M. *Science* **2004**, *303*, 655.
(6) Biercuk, M. J.; Garaj, S.; Mason, N.; Chow, J. M.; Marcus, C. M. *Nano Lett.* **2005**, *5*, 1267.
(7) Gräber, M. R.; Coish, W. A.; Hoffmann, C.; Weiss, M.; Furer, J.; Oberholzer, S.; Loss, D.; Schönenberger, C. *Phys. Rev. B* **2006**, *74* (7), 075427.
(8) Gräber, M. R.; Weiss, M.; Schönenberger, C. *Semicond. Sci. Technol.* **2006**, *21*, 64.
(9) Jørgensen, H. I.; Grove-Rasmussen, K.; Hauptmann, J. R.; Lindelof, P. E. *Appl. Phys. Lett.* **2006**, *89*, 2113.
(10) Wegewijs, M. R.; Nazarov, Y. V. *Phys. Rev. B* **1999**, *60*, 14318.
(11) Wegewijs, M. R.; Nazarov, Y. V.; Gurvitz, S. A. *Jpn. J. Appl. Phys.* **2001**, *40*, 1994.
(12) Waugh, F. R.; Berry, M. J.; Mar, D. J.; Westervelt, R. M.; Campman, K. L.; Gossard, A. C. *Phys. Rev. Lett.* **1995**, *75*, 705.
(13) Waugh, F. R.; Berry, M. J.; Crouch, C. H.; Livermore, C.; Mar, D. J.; Westervelt, R. M.; Campman, K. L.; Gossard, A. C. *Phys. Rev. B* **1996**, *53*, 1413.
(14) Schröer, D.; Greentree, A. D.; Gaudreau, L.; Eberl, K.; Hollenberg, L. C. L.; Kotthaus, J. P.; Ludwig, S. *Phys. Rev. B* **2007**, *76* (7), 075306.
(15) Brandes, T. *Phys. Rep.* **2005**, *408*, 315–474.
(16) Renzoni, F.; Brandes, T. *Phys. Rev. B* **2001**, *64* (24), 245301.
(17) Greentree, A. D.; Cole, J. H.; Hamilton, A. R.; Hollenberg, L. C. *Phys. Rev. B* **2004**, *70* (23), 235317.
(18) Michaelis, B.; Emary, C.; Beenakker, C. W. J. *Europhys. Lett.* **2006**, *73*, 677.
(19) Emary, C. *Phys. Rev. B* **2007**, *76*, 245319.
(20) Meier, F.; Levy, J.; Loss, D. *Phys. Rev. B* **2003**, *68* (13), 134417.
(21) Zhang, P.; Xue, Q.-K.; Zhao, X.-G.; Xie, X. C. *Phys. Rev. A* **2004**, *69* (4), 042307.
(22) Gaudreau, L.; Studenikin, S. A.; Sachrajda, A. S.; Zawadzki, P.; Kam, A.; Lapointe, J.; Korkusinski, M.; Hawrylak, P. *Phys. Rev. Lett.* **2006**, *97* (3), 036807.
(23) Korkusinski, M.; Puerto Gimenez, I.; Hawrylak, P.; Gaudreau, L.; Studenikin, S. A.; Sachrajda, A. S. *Phys. Rev. B* **2007**, *75*, 115301.
(24) Ihn, T.; Sigrist, M.; Ensslin, K.; Wegscheider, W.; Reinwald, M. *New J. Phys.* **2007**, *9*, 111.
(25) Stopa, M. *Phys. Rev. Lett.* **2002**, *88* (14), 146802.
(26) Vidan, A.; Westervelt, R. M.; Stopa, M.; Hanson, M.; Gossard, A. C. *Appl. Phys. Lett.* **2004**, *85*, 3602.
(27) Saraga, D. S.; Loss, D. *Phys. Rev. Lett.* **2003**, *90* (16), 166803.
(28) Zitko, R.; Bonca, J.; Ramsak, A.; Rejec, T. *Phys. Rev. B* **2006**, *73* (15), 153307.
(29) Javey, A.; Guo, J.; Wang, Q.; Lundstrom, M.; Dai, H. *Nature* **2003**, *424*, 654.
(30) Kim, W.; Javey, A.; Tu, R.; Cao, J.; Wang, Q.; Dai, H. *Appl. Phys. Lett.* **2005**, *87*, 3101.
(31) Babić, B.; Furer, J.; Iqbal, M.; Schönenberger, C. In *Electronic Properties of Synthetic Nanostructures: XVIII International Winterschool/Euroconference on Electronic Properties of Novel Materials*; Kuzmany, H., Roth, S., Mehring, M., Fink, J., Eds.; AIP Conference Proceedings 723; American Insitiute of Physics: Melville, NY, 2004; pp 574–582.
(32) Ilani, S.; Donev, L. A. K.; Kindermann, M.; McEuen, P. L. *Nat. Phys.* **2006**, *2*, 687.
(33) Bruus, H.; Flensberg, K.; *Many-body Quantum Theory in Condensed Matter Physics: An Introduction*; Oxford University Press: Oxford, 2004.
(34) Several gate switches were observed during measurements despite keeping the gate ranges very small. Figure 2 has therefore been translated along the gate axes $\Delta V_{Tg1} = -6.5$ mV and $\Delta V_{Tg1} = -1.5$ V to correct such switches relative to Figure 3.
(35) Condition for top-gate voltages Tg1–3. QD1: $V_{Tg1} = 1$ mV $\times \epsilon_1$–2 mV, $V_{Tg2} = -0.15$ V $\times \epsilon_1 + 3$ V ($N_2 = 1$), $V_{Tg3} = 16$ mV ($N_3 = 1$); QD2: $V_1 = 7$ mV ($N_1 = 1$), $V_{Tg3} = 16$ mV ($N_3 = 1$); QD3: $V_{Tg1} = 29$ mV ($N_1 = 2$), $V_{Tg2} = 1$ V $\times \epsilon_3 - 2$ V($N_2 = 3$), $V_{Tg3} = 10.5$ mV $\times \epsilon_3 - 3$ mV.
(36) The length between the contacts and the lengths of QD1–3 are $L \sim 1.4$ μm and L_{QDi}, $i = 1, 2, 3$, with $L_{QD2} \sim 1$ μm fixed (assuming the CNT crosses perpendicular to the contacts). The top-gates are made in a second electron beam lithography step aligning to predefined markers and we here assume a 100 nm shift (often observed) to the right relative to the contacts making QD3 small consistent with measurements (high charging energy U_{c3}). The estimated lengths of QD1 and QD2 therefore become $L_{QD1} \sim 0.3$ μm and $L_{QD3} \sim 0.1$ μm yielding backgate capacitances according to $C_{bg,i} = 2\pi\epsilon L_i/\ln(4\ h/d)$, where $\epsilon = 3.9\epsilon_0$ for Si oxide with height $h = 500$ nm and $d \sim 1$ nm is the diameter of the CNT.[32]
(37) The origin (0,0,0) of (V_{Tg1}, V_{Tg2}, V_{Tg3}) in the model is translated to (−5.5 mV, 0 V, 16 mV) to match the experimental voltages exactly in Figures 2 and 3. Furthermore, the model calculation in Figure 3 has been shifted by the addition of one electron in QD2, i.e., $-\Delta V_{Tg2} = -3.019$ V, since the model triple quantum dot is empty for negative voltages on V_{Tg2}.

NL072948Y